Applied Catalysis B: Environmental 176–177 (2015) 107–119

Contents lists available at ScienceDirect

Applied Catalysis B: Environmental

journal homepage: www.elsevier.com/locate/apcatb

FTIR and density functional study of NO interaction with reduced ceria: Identification of N_3^- and NO^{2-} as new intermediates in NO conversion

Mihail Y. Mihaylov[a], Elena Z. Ivanova[a], Hristiyan A. Aleksandrov[b], Petko St. Petkov[b], Georgi N. Vayssilov[b,**], Konstantin I. Hadjiivanov[a,*]

[a] Institute of General and Inorganic Chemistry, Bulgarian Academy of Sciences, Sofia 1113, Bulgaria
[b] Faculty of Chemistry and Pharmacy, University of Sofia, Sofia 1126, Bulgaria

ARTICLE INFO

Article history:
Received 5 February 2015
Received in revised form 22 March 2015
Accepted 29 March 2015
Available online 31 March 2015

Keywords:
Adsorption
Azides
Catalysis
Ceria
deNO$_x$
FTIR spectroscopy
Hyponitrites
NO
Nitric oxide dianion

ABSTRACT

To design new deNO$_x$ materials and processes we need to know in details the mechanism of NO interaction with solid surfaces. Many NO$_x$ conversion catalysts contain ceria as a component and cerium changes its oxidation state in the course of redox catalytic processes. Here we show that the interaction between NO and reduced ceria leads to formation of azides (N_3^-, 2044–2042 cm^{-1}) and nitric oxide dianion (NO^{2-}, 1010–980 cm^{-1}) with the simultaneous oxidation of Ce^{3+}. These species are established for the first time after NO adsorption on solid surfaces and their relative concentrations strongly depend on the sample morphology. At ambient temperature N_3^- does not interact with NO or O_2 alone but easily disappears in the co-presence of the two gases, thus demonstrating reactivity similar to that of isocyanates. In contrast, NO^{2-} accepts one NO molecule and is converted into hyponitrite (bands in the 1030–970 cm^{-1} region). At further stages of interaction, N_2O, N_2, nitrites and nitrates are formed. The present findings enrich the current opinions of catalytic NO conversion and impose some revisions.

1. Introduction

The post-combustion control of NO$_x$ emissions is a central problems in the environmental catalysis. As a result of the efforts of many research groups and industrial companies, different routes for catalytic NO$_x$ removal have been proposed and developed. Thus, the three-way catalysts were applied for mobile NO$_x$ sources [1] while selective catalytic reduction (SCR) by ammonia, for stationary sources [2]. SCR by hydrocarbons [2,3] and storage–reduction catalysts [4] have also been commercialized. The investigations on the direct NO decomposition are also topical. However, despite of the serious achievements, we still need more effective deNO$_x$-ing technologies.

To design new effective catalysts one should know in details the mechanisms of the processes occurring during interaction of NO$_x$ and different reducing agents on the surface. There are thousands of mechanistic studies dealing with various NO$_x$ conversion reactions. A very large part of them have been performed with vibrational spectroscopy because, in this way, one can obtain direct information on the nature of the surface species. However, the potential of the technique has not been fully explored and many assignments are still tentative and not proven by complementary techniques, such as isotopic labeling.

The formation of N—N bonds at a certain stage of the interaction is a common feature of all routes for catalytic NO conversion to N_2. Consequently, many of the proposed NO decomposition mechanisms consider neutral or charged dinitrosyl species [5–8]. Various mechanisms on the formation of dinitrogen during catalytic reduction involve coupling of two nitrogen-containing moieties with nitrogen in positive and negative formal oxidation state, respectively. Typical examples are NH_4NO_2 or NH_4NO_3 species proposed to be intermediates in the SCR of NO$_x$ with NH_3 [9,10]. Another example, concerning the reduction of NO$_x$ with hydrocarbons, is coupling between NCO^- and NO_2 [11,12].

* Corresponding author. Tel.: +359 29793598; fax: +359 28705024.
** Corresponding author. Tel.: +359 28161338; fax: +359 2962538.
E-mail addresses: gnv@chem.uni-sofia.bg (G.N. Vayssilov), kih@svr.igic.bas.bg (K.I. Hadjiivanov).

http://dx.doi.org/10.1016/j.apcatb.2015.03.054
0926-3373/

Table 1
Proposed assignments of IR bands observed after NO_x adsorption on ceria and related systems. The species are arranged according to the formal oxidation state of nitrogen. Data for N_2O are not included in the Table.

Species	System	Adsorbate	Characteristic IR bands, cm^{-1}	Refs.
Formal oxidation state of nitrogen 1+				
NO^-	CeO_2	NO	1176[a]	[19]
NO^-	CeO_2, MnO_x/CeO_2	NO + O_2	1180	[16]
NO^-	$Au/CeO_2–Al_2O_3$	NO + H_2	1176	[32]
NO^-	MnO_x/CeO_2	NO + O_2	1178	[33]
NO^-	$MnO_x–CeO_2–ZrO_2/\gamma–Al_2O_3$	NO[e]	1142	[48]
NO^- or chelating nitrite	CeO_2	NO	1174	[20]
NO^- and/or bidentate nitrite	$CeO_2–ZrO_2$	NO	1200–1185	[34]
trans-hyponitrite	CeO_2	NO	1105–1090[b]	[20–23]
trans-Hyponitrite	CeO_2	NO	1442, 1385	[19]
trans-Hyponitrite	CeO_2	NO + O_2	1422	[16]
trans-Hyponitrite	CeO_2/Al_2O_3	NO	1080	[22]
trans-Hyponitrite	MnO_x/CeO_2	NO + O_2	1406	[33]
trans-Hyponitrite	MnO_x/CeO_2	NO + O_2	1420, 1102	[16]
cis-Hyponitrite	CeO_2	NO	1015, 954[c]	[20]
cis-Hyponitrite	CeO_2	NO	1021, 974	[23]
cis-Hyponitrite	CeO_2	NO	1371, 1358	[19]
cis-Hyponitrite	CeO_2	NO + O_2	1350, 1013, 930	[16]
cis-Hyponitrite	MnO_x/CeO_2	NO + O_2	1350, 1011	[16]
cis-Hyponitrite	$CeO_2–ZrO_2$	NO + O_2	1360–1320, 1070–1040	[34]
cis-Hyponitrite	MnO_x/CeO_2	NO + O_2	1350, 1011	[16]
Hyponitrite	CeO_2	NO + CO	1360, 1080	[27]
Hyponitrite	$CeO_2–WO_3/TiO_2$	NO + O_2	1350	[35]
Hyponitrite	CuO/CeO_2 $CuO/CeO_2–ZrO_2$	NO	1387–1350	[36]
Hyponitrite	$Au/CeO_2–Al_2O_3$	NO + H_2	1300	[32]
Formal oxidation state of nitrogen 2+				
Dinitrosyl	CeO_2	NO	1910, 1840	[21]
Dinitrosyl	Ce-SAPO-18	NO	1843, 1749	[47]
Nitrosyl	$CeO_2–ZrO_2$	NO	1865	[37]
Nitrosyl	$CeO_2–ZrO_2$	NO + O_2	1940–1930	[34]
Nitrosyl	Ce-SAPO-18	NO	1912	[47]
Bent $NO^{\delta-}$	CeO_2-ZrO_2	NO	1753–1750	[37,38]
Bridging $NO^{\delta-}$	$CeO_2–ZrO_2$	NO	1200–1185	[37,38]
Formal oxidation state of nitrogen 3+				
Nitro species	sulfated CeO_2	NO + O_2	1500	[24]
Nitro species	$Ce_{0.6}Zr_{0.4}O_2$	NO + O_2	1449	[49]
Chelating nitro	CuO/CeO_2	NO	1281–1278	[36]
Chelating nitrite	CeO_2	NO	1162[d]	[23]
Chelating nitrite	CeO_2	NO	1277–75, 1167–65, 823	[20,23]
Chelating nitrite	CeO_2	NO	1270, 1165[b]	[21]
Chelating nitrite	CeO_2	NO + O_2	1275, 1165, 824	[25]
Chelating nitrite	CeO_2/Al_2O_3	NO	1171	[22]
Chelating nitrite	$MnO_x–CeO_2–ZrO_2/\gamma–Al_2O_3$	NO[e]	978, 907, 861, 834	[48]
Bidentate nitrite	CeO_2	NO	1184	[28]
Bidentate nitrite	CeO_2	NO + O_2	1184	[26]
Bidentate nitrite	CeO_2	NO + O_2	1160, 1105	[26]
Bidentate nitrite	$MnO_x–CeO_2–ZrO_2/\gamma–Al_2O_3$	NO[f]	1316	[48]
Monodentate nitrite	$MnO_x–CeO_2–ZrO_2/\gamma–Al_2O_3$	NO[e]	1399	[48]
Linear nitrite	$MnO_x–CeO_2–ZrO_2/\gamma–Al_2O_3$	NO[f]	1068	[48]
Linear nitrite	$MnO_x–CeO_2–ZrO_2/\gamma–Al_2O_3$	NO + O_2	1076	[48]
Nitrite	CeO_2	NO	1165, 1123	[29]
Nitrite	CeO_2	NO	141[g]	[23]
Nitrite	CeO_2	NO + CO	1280–1180	[27]
Nitrite	CeO_2	NO + O_2	1240	[16]
Nitrite	Ba/CeO_2	NO	1411, 1200	[39]
Nitrite	CeO_2/Al_2O_3	NO	1358	[40]
Nitrite	$CeO_2–TiO_2$	NO	1227	[41]
Nitrite	$Ce_{0.73}Zr_{0.27}O_2$, $Ce_{0.64}Zr_{0.27}Nd_{0.09}O_2$	NO + O_2	1350–1150	[46]
Nitrite or nitrate	$CeO_2–TiO_2$	NO	1557	[41]
Nitrite	$CeO_2–WO_3/TiO_2$	NO + O_2	1221	[35]
Nitrite	$MnO_x–TiO_2$	NO + O_2	1245	[16]
NO^+	$CeO_2–ZrO_2$	NO + O_2	2300–2200	[34]
HNO_2	$CeO_2–ZrO_2$	NO + O_2	3595–3570, 1700–1620, 1550–1300	[34]
Formal oxidation state of nitrogen 4+				
NO_2	$CeO_2–WO_3/TiO_2$	NO + O_2	1603	[35]
NO_2	$CeO_2–TiO_2$	NO	1615	[41]
NO_2	Ce-SAPO-18	NO	1625	[47]
NO_2	$MnO_x–CeO_2–ZrO_2/\gamma–Al_2O_3$	NO + O_2	1629	[48]

Table 1 (*Continued*)

Species	System	Adsorbate	Characteristic IR bands, cm^{-1}	Refs.
Formal oxidation state of nitrogen 5+				
Various nitrates	CeO_2	NO	1505, 1305, 1060	[20]
Various nitrates	CeO_2	NO	1608, 1575, 1535, 1305, 1276	[19]
Various nitrates	CeO_2	NO	1595-1500, 1275-1210, 1030-1000 1540, 1046, 744	[28]
Nitrate	CeO_2	NO	1585	[23]
Nitrate	CeO_2	NO	1535	[29]
Nitrate	CeO_2/Al_2O_3	NO	1642	[40]
Nitrate	CeO_2–TiO_2	NO	1378	[41]
Various nitrates	$Ce_{0.6}Zr_{0.4}O_2$	NO + O_{-2}	1609, 1566, 1538, 1277, 1242	[49]
Various nitrates	CuO/CeO_2	NO	1620–1606, 1573–1565, 1489–1479, 1227–1219, 1003	[36]
Various nitrates	Ba/CeO_2	NO	1590–1529, 1471–1308	[39]
Various nitrates	MnO_x–CeO_2–ZrO_2/γ–Al_2O_3	NO[f]	1590, 1549,1493, 1373, 1256, 1220	[48]
Bridged nitrate	CeO_2–TiO_2	NO + CO	1622	[42]
Various nitrates	CeO_2	NO + CO	1618–13, 1555–40, 1475–1457, 1280, 1245–1230, 1060–1000	[27]
Various nitrates	CeO_2	NO + O_2	1608–1528, 1278–1209	[24]
Various nitrates	CeO_2	NO + O_2	1595–1500, 1275–1210, 1030–1000	[26]
Various nitrates	CeO_2	NO + O_2	1626, 1540, 1046, 744	[15]
Various nitrates	CeO_2	NO + O_2	1608–1560, 1278–1209	[30]
Nitrate	CeO_2	NO + O_2	1530	[16]
Various nitrates	CeO_2–TiO_2	NO + O_2	1610, 1580, 1280, 1230	[43]
Various nitrates	CeO_2–ZrO_2	NO + O_2	1610–1480, 1295–1220, 1030–1005	[20]
Various nitrates	$Ce_{0.73}Zr_{0.27}O_2$, $Ce_{0.64}Zr_{0.27}Nd_{0.09}O_2$	NO + O_2	1650–1450, 1350–1150	[46]
Various nitrates	CeO_2–WO_3/TiO_2	NO + O_2	1582, 1510, 1440	[35]
Nitrate	MnO_x/CeO_2	NO + O_2	1614, 1530, 1290	[33]
Various nitrates	MnO_x/CeO_2	NO + O_2	1677, 1585, 1550, 1382, 1270, 1070	[16]
Various nitrates	MnO_x–CeO_2–ZrO_2/γ-Al_2O_3	NO + O_2	1593, 1498, 1393, 1365	[48]

[a] Observed only with reduced sample.
[b] The bands at 1270, 1165 and 1090 cm^{-1} are detected at 1250, 1140 and 1070 cm^{-1}, respectively, after adsorption of ^{15}NO [21].
[c] A contaminant band at *ca.* 1350 cm^{-1} suggested.
[d] The band decreases in intensity in the presence of O_2 at 473 K.
[e] Adsorption performed at 523 K.
[f] Adsorption performed at 423 K.
[g] Not detected in the presence of O_2.

Most of the deNO_x catalysts contain altervalent metal cations. During red-ox processes these cations, acting as catalytically active sites, change their oxidation state. Therefore, it is essential to know the nature of the species formed during NO interaction with reduced and oxidized materials. This is particularly important for the storage–reduction catalysts because NO_x initially interacts with their reduced forms.

Many catalysts for NO_x conversion, *e.g.*, three-way [13], storage reduction [14,15], selective catalytic reduction [16,17] and soot oxidation (by NO_x) catalysts [18] contain ceria. Important peculiarities of CeO_2 are its high oxygen storage capacity and easy reducibility [05]. There are many studies of the nature of the species formed during interaction of NO_x with ceria [05,17,19–31] and ceria-containing systems [05,16,32–49], and the proposed structures are summarized in Table 1. Based on the paper of Niwa et al. [21] and a more recent work of Martínez-Arias et al. [20], several authors reported formation of various species, such as NO^- [16,19,20,32–34,48], *cis*- and *trans*-hyponitrites [16,19–23,27,32–36], nitrites [16,20,21–23,25–29,34,35,39–41,46,48,50], and nitrates [15,16,19,20,23,24,26–30,33,35,36,39–43,46,48,49]. However, a careful inspection of the data in Table 1 indicates many controversial assignments. Unfortunately, only few isotopic studies have been performed in order to support some assignments. It was demonstrated [21] that bands at 1270 and 1160 cm^{-1} (assigned to chelating nitrites) and a band at 1090 cm^{-1} (attributed to *trans*-hyponitrites) were due to N—O modes because were accordingly shifted after adsorption of ^{15}NO. Szanyi and Kwak [50] recently reported that $^{15}NO_2^-$ nitrite species (1153 and 815 cm^{-1}) absorb at 1137 and 798 cm^{-1} after substitution of one of the ^{16}O atoms by ^{18}O. It is established that the deNO_x activity of ceria correlates with the number of oxygen vacancies [17]. However, little attention has been paid to the surface species formed on reduced samples: NO^-, *trans*- and *cis*-hyponitrites and nitrates were mainly reported [17,19,31].

In this work we report the results of a careful investigation of the species arising after interaction between NO and reduced ceria. In order to distinguish between the properties typical of the oxide and the morphology effects we have studied two different samples. The main techniques utilized were FTIR spectroscopy of adsorbed ^{14}NO, ^{15}NO, and $^{14}NO + {}^{15}NO$ isotopic mixtures and periodic density functional (DF) calculations.

Successive adsorption of small NO doses allowed to distinguish different species and to follow the order of their formation. The band at 2118 cm^{-1}, characterizing the $^2F_{5/2} \rightarrow {}^2F_{7/2}$ electronic transition band of Ce^{3+}, was used to follow the reduction degree of ceria [51]. The significant difference between the $^{15}N/^{14}N$ isotopic shift factors for N—N and N—O bonds [52] allowed unambiguous assignments of particular IR bands to N—N or N—O modes. Finally, adsorption of isotopic mixtures permitted to check for existence of N—O modes coupled *via* N—N bonds.

We provide spectral evidences of the formation of azide (N_3^-) and nitric oxide dianion (NO^{2-}) surface species during the initial stages of NO adsorption on reduced ceria. The further interaction of these species with NO_x was also studied and formation of surface hyponitrites, N_2O, nitrites and nitrates was established. The observations enrich the current opinions on the mechanisms of catalytic NO conversion.

2. Experimental

2.1. Samples

The CeO_2(A) sample originated from Rhodia (France) and had a specific surface area of 170 m^2g^{-1}. The CeO_2(B) sample had a simi-

lar specific surface area (173 $m^2 g^{-1}$) and was supplied from Daiichi Sankyo (Japan).

2.2. Experimental techniques

The IR investigations were performed using a Nicolet 6700 spectrometer equipped with a MCT detector at a spectral resolution of 2 cm^{-1} and accumulating up to 128 scans. Self-supporting pellets (≈10 mg cm^{-2}) were prepared by pressing the sample powders at 100 kPa, and the pellets were directly analyzed in a purpose-made IR cell. The latter was connected to a vacuum apparatus with a residual pressure of 10^{-4} Pa. Prior to each series of experiment the samples were activated by heating at 773 K for 1 h in oxygen (20 kPa) and evacuation for 1 h at the same temperature. Then, the samples were reduced with hydrogen (150 kPa) for 1 h at 773 K, followed by 1 h evacuation at the same temperature. These procedures were repeated three times in order to minimize the amount of residual carbonates that are always present on activated ceria. Nitrogen monoxide (>99.5% purity), O_2 (>99.999%) and H_2 (>99.999%) were purchased from Messer. ^{15}NO (>99% isotopic purity) was supplied by Isotec Inc., and was diluted in He (molar ratio of NO:He = 1:10). NO was additionally purified by fraction distillation. Oxygen and hydrogen were additionally purified by passing through a liquid nitrogen trap. The TEM investigations were performed on a TEM JEOL 2100 instrument at accelerating voltage of 200 kV.

2.3. Computational details

The calculations are performed using a periodic plane-wave DFT method with PW91 exchange–correlation functional of a generalized-gradient (GGA) type as implemented in the VASP program [53]. The stoichiometric and reduced ceria is described within the so-called GGA + U approach, in which on-site Coulombic interaction with $U = 4$ eV is included. The kinetic energy cut-off is 415 eV. The calculations are performed as spin-polarized, where appropriate. Ceria is modeled as a stoichiometric nanoparticle $Ce_{21}O_{42}$ with a diameter of 1.0 nm and it exhibits the crystallinity of the fluorite structure of CeO_2 that was previously used for the modeling of nanostructured ceria systems [53–55]. The space between neighboring slab images is 1.0 nm, which ensures that the lateral interactions between the supported clusters are insignificant. The $CeO_2(111)$ surfaces are modeled with a slab $Ce_{54}O_{108}$ of three CeO_2 (eighteen atomic) layers and a 3×6 surface cell. Calculations including only the Γ-point, appropriate for finite models, are considered accurate enough for the studied slab models with rather large surface unit cells. Complete geometry optimization has been performed for the nanoparticle and slab models. The stability of the formed species was evaluated by the adsorption energy (Table 2), with respect to corresponding number of NO molecules and reduced ceria models (see Supporting information).

The harmonic vibrational frequencies of the adsorbed N-containing species are calculated numerically. To account for anharmonicity and the computational method, the calculated vibrational frequencies are scaled by a factor of 0.952 and 0.980 for the N—N and N—O modes, respectively. The scaling factors are determined from the calculated and experimental frequencies in the gas phase of NO, N_2O, N_2, and HN_3.

3. Results and discussion

3.1. Initial characterization of the samples and background spectra

The TEM images revealed the average particle size of about 5 and 1 nm for the CeO_2(A) and CeO_2(B) samples, respectively. The

Table 2
Calculated adsorption energy of NO when N_3^- species are formed on reduced ceria nanoparticles (species a, b, d and e) and on reduced $CeO_2(111)$ slab (species c), E_{ads} in eV, and characteristic experimental and calculated vibrational frequencies of the species.

Species	E_{ads}(NO), eV[a]	ν, cm^{-1}	Ov_{in}/Ov_{in}[b]	Ce^{3+},[c]	Isotopic shifts (cm^{-1}) for the of vibrational modes of N_3^- species after substitutions of ^{14}N atoms by ^{15}N					
					$^{15}N^{14}N^{14}N$	$^{14}N^{14}N^{15}N$	$^{14}N^{15}N^{14}N$	$^{15}N^{14}N^{15}N$	$^{15}N^{15}N^{14}N$	$^{14}N^{15}N^{15}N$	$^{15}N^{15}N^{15}N$
$[N_3^-]$ (exp.)	–	2044–42	–	–	−11	−11	−22	−45	−56	−56	−67
$[N_3^-]$-a	−7.39	2033	4/1	8/1	−10	−10	−22	−46	−57	−57	−69
$[N_3^-]$-b	−7.75	2033	4/1	8/1	−10	−10	−22	−46	−57	−57	−69
$[N_3^-]$-c	−10.91	2002	4/1	8/1	−11	−11	−22	−45	−56	−56	−68
$[N_3^-]$-d[d]	−7.11	2062	4/1	8/1	−7	−14	−45	−23	−52	−60	−69
$[N_3^-]$-e[e]	−6.66	2021	4/1	8/1	−5	−20	−45	−25	−49	−66	−70

[a] E_{ads}(NO) is calculated with respect to the three NO molecules in the gas phase and reduced ceria with the number of O vacancies shown in the column Ov_{in}.
[b] The number of O vacancies in the model before the adsorption of NO and after the formation of the adsorbed species.
[c] The number of Ce^{3+} ions in the model before the adsorption of NO and after the formation of the adsorbed species.
[d] In structure $[N_3^-]$-d the three NNN atoms in the azide species are in the following order: the atom bound to two cerium ions, the middle N atom, and the terminal N atom.
[e] In structure $[N_3^-]$-e the three NNN atoms in the azide species are in the following order: the atom bound to cerium ions, the middle N atom, and the N atom bound to one cerium ion.

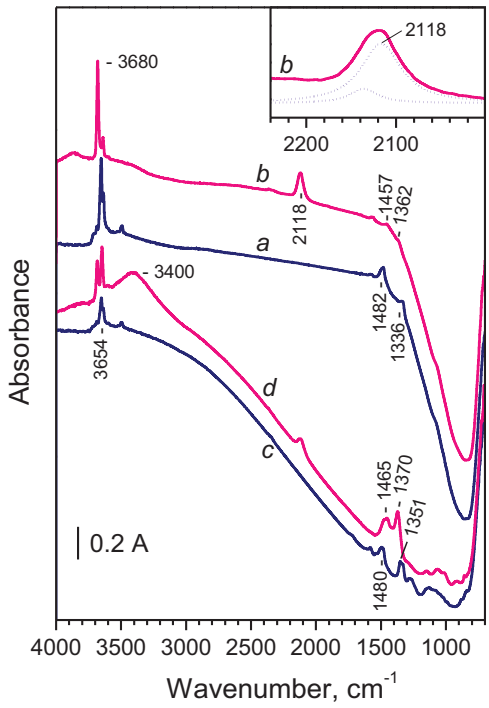

Fig. 1. FTIR spectra of activated (a and c) and reduced (b and d) CeO_2(A) (a and b) and CeO_2(B) (c and d) samples. The inset shows the region of the $^2F_{5/2} \rightarrow {}^2F_{7/2}$ electronic transitions of the Ce^{3+} ions.

crystal structure of both samples is cubic of fluorite-type oxides. The similar specific surface areas of the samples, compared with the particle size, indicates a substantial surface roughness of the CeO_2(A) sample.

The spectra of the activated and reduced ceria samples are presented in Fig. 1. Compared to other oxides, ceria is highly transparent in the low-frequency region. Thus, the so-called "cut-off" of our samples is around 700 cm^{-1}, *i.e.*, we were able to detect bands down to this wavenumber. This is important because many nitrogen-oxo species manifest bands at low frequencies that cannot be detected with many other catalysts due to the sample own absorbance. Consistent with the larger size of the particles, the spectrum of the CeO_2(A) sample is characterized by a higher light-scattering at high wavenumbers.

Activated ceria samples (Fig. 1, spectra a, c) are characterized by bands in two regions: 3700–3450 cm^{-1} (surface OH groups [56]) and 1600–1000 cm^{-1} (carbonate-like structures [20,21,55]). The bands registered in the OH region (see Fig. S1 from the Supplementary content for more details) are consistent with earlier reports [55–60]. In particular, the weak bands at 3712 and 3687 cm^{-1} are assigned to type I hydroxyls (*i.e.*, the oxygen atom is bound to one cerium cation) [34,51,57–59]. The most intense band at 3654 cm^{-1} is due to hydroxyls of type II-A and the satellite at 3636 cm^{-1}, to type II-B bridging OH groups (*i.e.*, the oxygen atom is bound to two cerium cations) [55–60]. The weak band at 3495 cm^{-1} has been attributed to cerium hydroxide microphase [57] or to type III hydroxyls [59,60]. We prefer the latter assignment because these species disappeared after reduction (see below) and re-appeared again after subsequent oxidation of the samples.

Several bands of low intensity (maxima at 1592, 1480, 1351, 1330, 1282, 1263 and 1077 cm^{-1}) are observed with the oxidized CeO_2(B) sample (Fig. 1, spectrum c) and are assigned to residual carbonate structures that are normally present on activated ceria samples [20,21,55]. These bands are definitely more intense with samples that were only evacuated at 773 K but strongly decreased in intensity after three oxidation and two reduction procedures (see Experimental 2). With the CeO_2(A) sample the carbonate bands are even weaker (Fig. 1, spectrum a) and maxima at 1573, 1482, 1336 and *ca.* 1070 cm^{-1} are observed. We imply that carbonates are located at subsurface layers because their bands (i) are hardly affected by adsorbed molecules, (ii) resist isotopic exchange with $^{13}CO_2$ and (iii) decrease in concentration only after oxidation/reduction treatments.

It is reported that with increasing degree of reduction the II-A OH band is gradually shifted to 3684 cm^{-1} and the II-B band, to 3651 cm^{-1} [17,51,57,58]. In agreement with these reports, after reduction of our samples the spectrum in the OH region changes, and the type II OH bands (3654 and 3636 cm^{-1}) are shifted to 3680 and 3639 cm^{-1}, respectively, for the CeO_2(A) sample and to 3684 and 3647 cm^{-1}, respectively, for the CeO_2(B) sample (see Fig. S1 from the Supplementary content). The band at 3495 cm^{-1} disappeared and intense broad band at 3400 cm^{-1} (Fig. 1) was observed with the sample CeO_2(B). This band has been attributed to H-bonded hydroxyls with a possible internal location [56]. The results indicate slightly more efficient reduction with the CeO_2(B) sample.

Reduction also affects the carbonate bands. Two bands at 1465 and 1370 cm^{-1} are well distinguished with the reduced CeO_2(B) sample (Fig. 1, spectrum d). The positions are consistent with earlier reports [55]. The intensities of the carbonate bands with the reduced CeO_2(A) sample are negligible (Fig. 1, spectrum b) showing that in this case the ceria sample was almost carbonate-free.

Finally, a band at 2118 cm^{-1} with a weak shoulder at 2134 cm^{-1} is detected only with the reduced samples (Fig. 1, spectra b, d and the inset). It is due to the $^2F_{5/2} \rightarrow {}^2F_{7/2}$ electronic transitions of the Ce^{3+} ions formed during the reduction [51].

Successive adsorption of small doses of oxygen on the reduced samples leads, in general, to gradual transformation of the spectra to spectra typical of oxidized materials (not shown). This causes the appearance of different pseudo-bands that are more pronounced with the CeO_2(B) sample, probably due to the more important carbonate content.

3.2. Initial stages of $^{14}NO/^{15}NO$ interaction with reduced ceria

Figs. 2 and 3 show the development of the FTIR spectra after successive adsorption of small doses of NO and ^{15}NO on the reduced CeO_2 samples. There are only two groups of IR bands that are sensitive to the $^{14}N/^{15}N$ substitution, their maxima being at 2044–2042 cm^{-1} and at 1010–980 cm^{-1}, respectively. Some negative bands are also observed (*e.g.*, a band at 923 cm^{-1} in Fig. 3, panel B). These bands are not sensitive to the isotopic substitution and are due to changes in the ceria background.

It is also seen that with the two samples the bands appear with strongly different relative intensities. Thus, the bands in the 1010–980 cm^{-1} region are of similar intensity for the two samples while the band at 2044–2042 cm^{-1} is by more than one order of magnitude more intense with the CeO_2(A) sample. This indicates that (i) the bands in the two spectral regions belong to different species and (ii) different surface sites are involved in the formation of these species. In parallel with the development of surface nitrogen-containing species, ceria is oxidized as seen by the parallel decrease in intensity of the band at 2118 cm^{-1} due to Ce^{3+} electronic transition. These observations strongly indicate reduction of NO and suggest that the formal oxidation state of nitrogen in the species formed is lower than 2. It should be also noted that the species under consideration were not formed when NO was adsorbed on non-reduced (activated) ceria samples.

Another effect of NO adsorption is the change of the spectra in the OH region (see Fig. S2 from the Supplementary content). The hydroxyl bands typical of reduced state are gradually eroded and bands at lower frequencies, characteristic of the oxidized material, developed at their expense. These results confirm the oxidation of

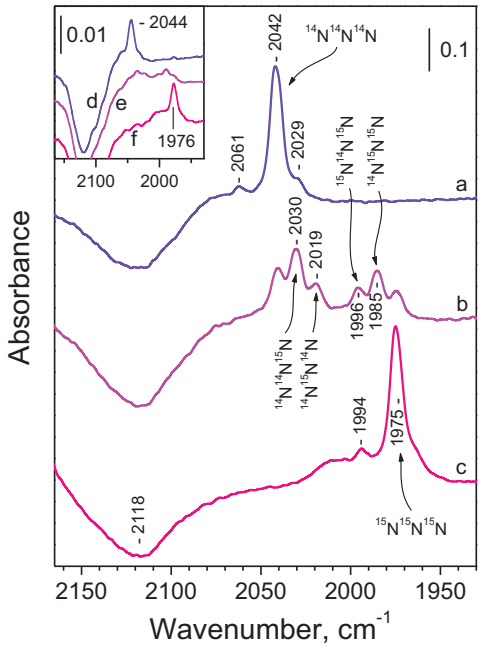

Fig. 2. FTIR spectra of ^{14}NO (a), $^{14}NO + ^{15}NO$ (b) and ^{15}NO (c) adsorbed onto the reduced CeO_2(A) sample. The amount of NO is 150 μmol g^{-1} CeO_2. The inset shows analogous spectra for the CeO_2(B) sample (85 μmol NO g^{-1} CeO_2): adsorption of ^{14}NO (d), $^{14}NO + ^{15}NO$ (e) and ^{15}NO (f).

ceria by NO and indicate that, at least at low coverage, the hydroxyls are not involved in the formation of the N-containing species. Other bands sensitive to the isotopic substitution are formed only at higher coverage and will be discussed latter.

Bands in the 1030–980 cm^{-1} region have already been registered after NO adsorption of ceria-containing systems and consensually assigned to *cis*-hyponitrite species [16,20,23]. Note however, that those bands were registered with non-reduced materials, which makes the direct analogy with our results doubtful. In contrast, the band at 2044–2042 cm^{-1} has not been reported by other authors. In what follows we shall consecutively consider the two spectral regions.

3.3. Species with characteristic bands at 2044–2042 cm^{-1}

The isotopic shift factor is a reliable criterion for distinguishing different types of bonds. It can be easily calculated on the basis of harmonic diatomic oscillator model and is generally valid for the stretching modes of polyatomic molecules [52]. Due to the anharmonicity of the bond vibrations, small deviations are observed with real systems. However, these deviations are relatively important only for H/D exchange and are small for other isotopic substitutions [52].

Theoretical isotopic shift factors, calculated on the basis of harmonic diatomic oscillators, are 1.035 for $\nu(^{14}N{-}^{14}N)/\nu(^{15}N{-}^{15}N)$ and 1.018 for $\nu(^{14}N{-}O)/\nu(^{15}N{-}O)$ substitutions [52]. The isotopic shift factor of the 2044–2042 cm^{-1} band is 1.034, implying that it characterizes nitrogen–nitrogen bond(s). Upon adsorption of a 1:1 $^{14}NO + ^{15}NO$ isotopic mixture, the band appears as a sextet (see panels C and D in Fig. 2) and the maxima for the CeO_2(A) sample are detected at 2041, 2030, 2019 1996, 1985 and 1974 cm^{-1}. Note also that the bands at 2030 and 1985 cm^{-1} are *ca.* 2 times more intense than the other bands.

If the species under consideration contained one N—N bond, adsorption of equimolar $^{14}NO + ^{15}NO$ isotopic mixture should lead to production of equal amounts of $^{14}N{-}^{14}N$, $^{14}N{-}^{15}N$, $^{15}N{-}^{14}N$, and $^{15}N{-}^{15}N$ species, *i.e.*, maximum 4 bands should be observed in

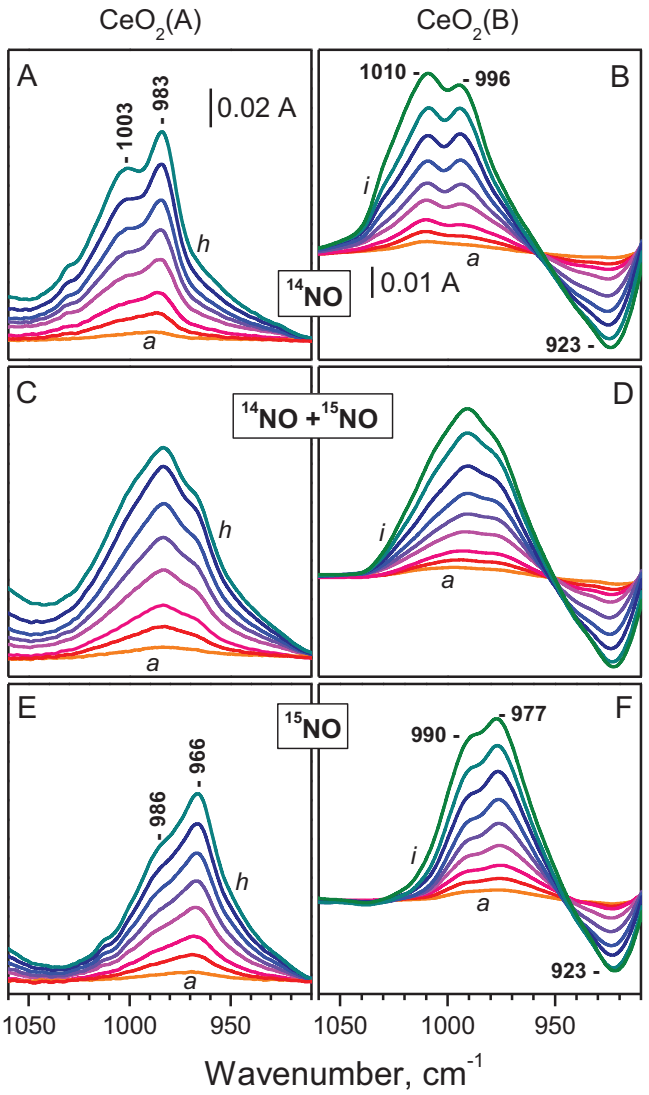

Fig. 3. FTIR spectra of ^{14}NO (A and B), $^{14}NO + ^{15}NO$ (C and D) and ^{15}NO (E and F) adsorbed onto the reduced CeO_2 samples. Sample CeO_2(A) (A, C and E), sample CeO_2(B) (D, D and F). The spectra are background corrected. Successive adsorption of small NO doses is shown for both samples. Sample CeO_2(A): 1 (a), 3 (b), 5 (c), 8 (d), 11 (e), 14 (f), 17 (g) and 20 (h) doses, each of 7.6 μmol g^{-1}. Sample CeO_2(B): 2 (a), 4 (b), 6 (c), 9 (d), 12 (e), 15 (f), 18 (g), 21 (h) and 24 (i) doses, each of 7.0 μmol g^{-1}. The Y-axes scales are equal for each sample.

the spectra. Therefore, the results indicate that the species contain more than one N—N bonds.

Consider species containing N—N—N fragments. Statistically, equal amounts of the following eight species should be produced after adsorption of 1:1 isotopic mixture: $^{14}N{-}^{14}N{-}^{14}N$, $^{15}N{-}^{14}N{-}^{14}N$, $^{14}N{-}^{15}N{-}^{14}N$, $^{14}N{-}^{14}N{-}^{15}N$, $^{14}N{-}^{15}N{-}^{15}N$, $^{15}N{-}^{14}N{-}^{15}N$, $^{15}N{-}^{15}N{-}^{14}N$ and $^{15}N{-}^{15}N{-}^{15}N$. However, if the species are symmetric, the $^{15}N{-}^{14}N{-}^{14}N$ and $^{14}N{-}^{14}N{-}^{15}N$ structures will be equivalent and the same accounts for the $^{14}N{-}^{15}N{-}^{15}N$ and $^{15}N{-}^{15}N{-}^{14}N$ structures. Therefore, in this case six different species will be observed and the species having one terminal nitrogen atom differing from the others by atomic weight will be in highest concentration.

The intensities of the bands in the experimentally observed sextet follow a statistical distribution consistent with highly symmetric species with two equivalent and one different nitrogen atoms. Based on these result, and in agreement with literature data [61–64] the 2044–2042 cm^{-1} band is assigned to the antisymmetric $^{14}N{-}^{14}N{-}^{14}N$ stretching modes of azide species, $^{14}N_3{}^-$

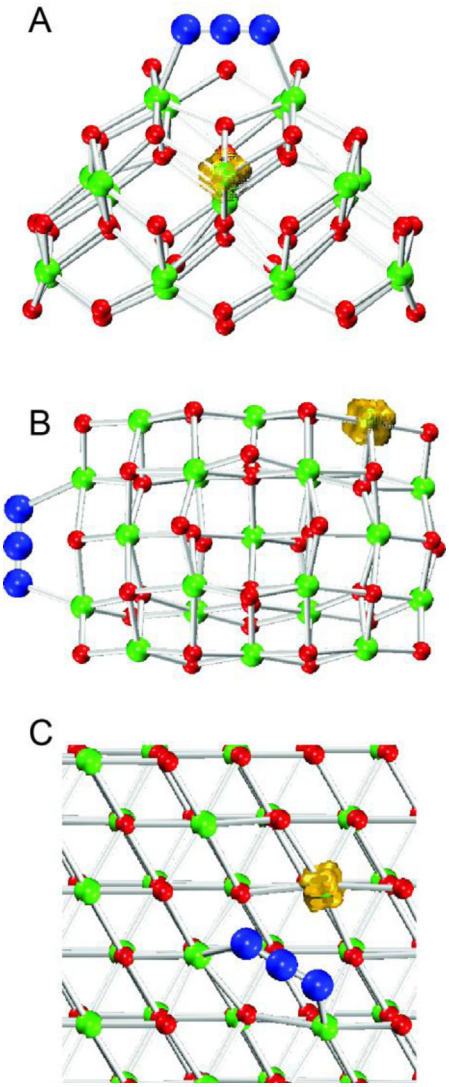

Fig. 4. Optimised structures of N_3^-. The azide structures, obtained with DFT modeling, are: structures [N_3^-]-a (panel A) and [N_3^-]-b (panel B) on the nanoparticle and [N_3^-]-c (panel C) on CeO_2(1 1 1) surface (colour coding: dark blue – nitrogen, red – oxygen, light green – cerium, yellow – unpaired electron density). (For interpretation of the references to color in this figure legend, the reader is referred to the web version of this article.)

(16-electron structure, formal oxidation state of nitrogen −1/3) [65]. The symmetric stretching modes are IR inactive but could be observed with surface species as a result of distorted symmetry. Here analogy with CO_2 (isoelectronic with N_3^-) could be helpful. After adsorption on positively charged sites CO_2 is normally coordinated *via* one of its oxygen atoms which leads to significant symmetry reduction. Consequently, some authors have observed the ν_s mode of adsorbed CO_2 in the IR spectra [66,67]. However, the respective band is of very low intensity and can be observed at high CO_2 coverages only. In our case the symmetry reduction of azides (see Fig. 4) is lower as compared to adsorbed CO_2 which should reflect in even lower intensity of the ν_s band. The ν_s mode of azide species is expected around 1350 cm^{-1} [63,64]. However, we have observed no bands assignable to azides in this region, *i.e.*, if any, the ν_s band remains with too low intensity. This confirms the high symmetry of surface azides consistent with the proposed structures.

Formation of surface azides has been suggested by other authors [68,69], however after NH_3 oxidative adsorption on various catalysts. The structure of these species has not been proven by isotopic studies. According to our results N_3^- can be produced as a result of NO reductive adsorption.

In order to check the assignment of the bands and the isotope shifts we performed series of DFT calculations for azide species on ceria (for details see Fig. S3 from the Supplementary content and the corresponding text). Two of the modeled structures on the ceria nanoparticle (Fig. 4, panels A and B) possess the high symmetry suggested by the analysis of the experimental spectra. The calculated vibrational frequency of those species, 2033 cm^{-1}, is close to the experimental frequencies assigned to N_3^- species (see Table 2). Moreover, we found an excellent quantitative agreement between the experimental frequency shifts for N_3^- moiety formed after adsorption of the $^{14}NO + {}^{15}NO$ mixture (see above) and the calculated shifts of the species with different arrangements of ^{14}N and ^{15}N isotopes in the azide species. Note that the N_3^- structures with high symmetry are formed at the edges of the ceria nanoparticle. We also modeled N_3^- structures on the CeO_2(1 1 1) surface (see Fig. 4, panel C). This species has vibrational frequency of 2002 cm^{-1}, *i.e.*, by 31 cm^{-1} lower than the values calculated for the azides on ceria nanoparticles. The simulated isotopic shifts with the species on CeO_2(1 1 1) surface also fit very well to the experimentally observed bands (Table 2). Indeed, weak satellite bands at 2061 and 2029 cm^{-1} are visible in the spectra shown in Fig. 2, panel A, These satellites could be due to some heterogeneity of azides arising from their different locations at edges or facets of ceria particles, as suggested by the density functional calculations.

From stoichiometric point of view the formation of N_3^- includes interaction of three NO molecules with reduced ceria sample that results in filling of three oxygen vacancies and simultaneous oxidation of seven Ce^{3+} ions to Ce^{4+}, as shown schematically in Eq. (1):

$$3[-Ce^{3+}-\square-Ce^{3+}-] + Ce^{3+} + 3\,NO \rightarrow 3[-Ce^{4+}-O^{2-}-Ce^{4+}-] + Ce^{4+} + N_3^- \quad (1)$$

Since the formation of symmetric azide anions includes healing of three oxygen vacancies and the creation of two N—N bonds, the process is highly exothermic, with a calculated reaction energy, Er, of −7.39 to −7.75 eV on ceria nanoparticle and −10.91 eV on CeO_2(1 1 1) surface (Table 2). The reaction energy on the regular surface is higher in absolute terms due to the higher energy of formation of oxygen vacancy on the planes [53,54]: the energy for filling three oxygen vacancies on the regular (1 1 1) surface is −8.94 eV, while on ceria nanoparticle the corresponding value is calculated to be −5.82 eV.

3.4. Reactivity of surface azides

The azide and the isocyanate anions are isoelectronic. Several authors [11,12,70] reported that NCO^- species are intermediates in the selective catalytic reduction of NO_x with hydrocarbons. The isocyanates are thermally stable and hardly interact with NO or O_2 alone. However, these species disappear in mixtures of the two gases with the formation of dinitrogen [11,12]. Here we found a very similar behavior of the surface azides. They are thermally stable (decompose above 573 K) and practically does not interact with NO (at low equilibrium pressure) or O_2 at ambient temperature. However, the azides disappear quickly when small amount of O_2 were added to NO preliminary present in the system. Simultaneously, nitrito- and nitrato-species were produced. No intermediate species with an IR active N—N bond are formed during interaction of azides with $NO + O_2$ as can be seen in Fig. S4 from the Supplementary content. It is also to be noted that azides decrease in concentration under high NO equilibrium pressures because at these conditions some NO_2 is formed [71].

The similar chemical properties of N_3^- and NCO^- suggest that azides are intermediates in the formation of dinitrogen. Indeed, it is known that azides can interact with HNO_2 (formal oxidation state of nitrogen 3+) to yield N_2 and N_2O *via* formation of nitrosyl azide as an intermediate [63].

3.5. Species with characteristic bands at 1010–980 cm^{-1}

Analysis of the intensities of the azide IR bands presented in Fig. 2 shows that there is no straight correlation between the formation of these species and the negative band at 2118 cm^{-1} quantifying the amount of Ce^{3+} ions in the samples. This is due to another process leading to ceria oxidation, namely the formation of species absorbing in the 1010–980 cm^{-1} region.

The two bands, at 1003 and 983 cm^{-1}, shown in Fig. 3, panel A (sample CeO_2(A)), change almost in concert which could suggest they characterize one species. However, detailed analysis indicates the band at 983 cm^{-1} develops somewhat faster than the band at 1003 cm^{-1}. Similar is the situation with the two bands (at 1010 and 996 cm^{-1}) observed with the CeO_2(B) sample (Fig. 3, panel B). Moreover, the intensity ratio between the lower- and the higher-frequency bands for the two samples is markedly different. This implies that each of the bands around 1000 cm^{-1} characterizes different individual species. The conclusion is further supported by the spectra presented in Fig. S5 from the Supplementary content. It is seen that the two bands are observed with different intensity ratio (and at slightly different wavenumbers) when the CeO_2(A) sample was subjected to different pretreatments. The band at 983 cm^{-1} disappears from the spectra after evacuation of the sample at 473 K, while the band at 1003 cm^{-1} demonstrates a slightly higher stability: a temperature of 523 K is needed for decomposition of the respective species.

The $^{14}N/^{15}N$ isotopic shift factor for all bands in the 1010–980 cm^{-1} region is 1.019–1.020. Analysis of summarized literature data [52,71,72] shows that the $\nu(^{14}N{-}O)/\nu(^{15}N{-}O)$ isotopic shift factor is observed in the interval of 1.014–1.022 with few exceptions down to 1.012. Therefore, the results imply the bands characterize $^{14}N{-}O$ stretching modes.

It is important to underline that no contaminant bands developed in parallel with the bands in the 1010–960 cm^{-1} region. This observation excludes the possible assignment of the bands to nitrates, nitrites or nitro-species. Indeed, all these species are characterized by at least two N—O stretching modes and also manifest bent modes in the 900–750 cm^{-1} region. Note also that the formal oxidation state of nitrogen in these species is >2 which contradicts to the conclusion that the species formed are products of NO reduction.

As already noted, bands in this region have been usually attributed to *cis*-hyponitrites [16,20,23] (see also Table 1). However, using the above arguments (no contaminant bands) we can exclude the bands in the 1010–980 cm^{-1} region to characterize *cis*-hyponitrite species because the latter manifest two NO modes (ν_s at 1047 and ν_{as} at 830 cm^{-1} for bulk species) [72]. Therefore, the two possible assignments of the bands under consideration are to isolated ^{14}NO moieties or to highly symmetric nitrogen-oxo anions, as *trans*-hyponitrites, where only the ν_{as}(NO) modes are IR active.

Consider first the possible assignment to *trans*-hyponitrite structures ($N_2O_2^{2-}$ or $N_2O_2^-$). Because of the high symmetry, the N—N and the symmetric N—O modes are not IR active and ν_{as}(N—O) should be the only IR band in the accessible frequency region, *i.e.*, above 700 cm^{-1}. For bulk *trans*-hyponitrites the ν_{as} band is detected at 1031 cm^{-1} [72], *i.e.*, at a position close to the bands observed by us. Upon ^{15}N substitution the band is shifted to 1015 cm^{-1}. However, for partly substituted species, $[O^{14}N^{15}NO]^{2-}$, the band is observed at 1022 cm^{-1} [72].

Absorption of a 1:1 $^{14}NO + ^{15}NO$ isotopic mixture should results in 50% of the species with $[O^{14}N^{15}NO]^{2-}$ isotopic composition. Therefore, if the species were symmetric *trans*-hyponitrites, two bands around 995 and 975 cm^{-1} should dominate in the spectra of isotopic mixture adsorbed on the CeO_2(A) sample and at 1000 and 987 cm^{-1} for the CeO_2(B) sample. However, no such bands are produced in the real spectra (this is well seen in Fig. S6 from the Supporting information where the second derivatives of the spectra are presented). In contrast, the spectra of adsorbed isotopic mixture coincide well with the average of the spectra registered after ^{14}NO and ^{15}NO alone. Therefore, the isotopic studies allow rejecting the possibility the species to possess a hyponitrite structure. Thus, the results imply the bands in the 1010–980 cm^{-1} region produced during the initial stages of interaction of NO with reduced ceria are due to isolated N—O modes.

The stretching frequency of diatomic ^{14}NO entities reflects the $^{14}N{-}O$ bond order (see Fig. S7 from the Supplementary content). Thus, $^{14}NO^+$ (2345 cm^{-1}), ^{14}NO (1876 cm^{-1}) and $^{14}NO^-$ (1374 cm^{-1}) have bond orders of *ca.* 3, 2.5 and 2, respectively [72]. The low frequency allows us to attribute the band at 1010–980 cm^{-1} to the N—O stretching modes of $^{14}NO^{2-}$ ions (N—O bond order of *ca.* 1.5). Indeed, a very similar Raman stretching frequency (951 cm^{-1}) was recently reported for $^{14}NO^{2-}$ species produced after interaction between NO and N_2^{3-} in a di-yttrium complex [73]. The frequency of the respective $^{15}NO^{2-}$ species was reported at 935 cm^{-1} (isotopic shift factor was 1.017) [73].

No formation of NO^{2-} species has been considered in the surface chemistry. One of the reasons for this is the relatively low stretching frequency of NO^{2-} which makes impossible its detection with most catalytic systems. In addition, few of the NO adsorption investigations have been performed with reduced samples, a condition necessary for the formation of NO^{2-}.

The NO^{2-} species were also modeled computationally on a reduced support for different locations on the ceria nanoparticle or on CeO_2(1 1 1). They were formed when the NO moiety was situated between two cerium cations, in the $\eta^2{:}\eta^2$ position (see Fig. 5, panels A–C), as in the di-yttrium complex reported recently [73]. The calculated vibrational frequencies of the $^{14}NO^{2-}$ species on ceria nanoparticles are 993–979 cm^{-1} (Table 2). The highest wavenumber band (993 cm^{-1}) corresponds to the most stable species ($E_r = -1.35$ eV) which is in agreement with the experimental observations. The vibrational frequency of the $^{14}NO^{2-}$ species on the CeO_2(1 1 1) face was calculated at the slightly higher position of 1005 cm^{-1}. Thus, the experimentally observed higher-frequency bands could be associated with species on regular crystal planes.

Therefore, $[NO]^{2-}$ is produced according to the reaction:

$$-Ce^{3+}{-}\square{-}Ce^{3+}- + NO \rightarrow -Ce^{4+}{-}[NO]^{2-}{-}Ce^{4+}-, \quad (2)$$

i.e., the oxygen vacancy is filled by doubly charged NO moiety instead of O^{2-}.

According to the DFT studies, when the NO moieties are not located between two cerium cations, monoanionic NO^- species could be formed on reduced samples (see Fig. S8 from the Supplementary content). Those species are notably less stable than $^{14}NO^{2-}$, $E_r = -0.45$ eV, and the calculated frequency for $^{14}NO^-$ is considerably higher than for NO^{2-}, in the 1454–1435 cm^{-1} region (see structures $[NO^-]$-a and $[NO^-]$-b in Table 3; other types of NO^- species with even lower stability are described in the Supplementary content). However, we have not detected bands assignable to $^{14}NO^-$ in the FTIR experiments, which indicates that these species are not formed at the earlier stages of interaction between reduced ceria and ^{14}NO most probably due to their low stability. Note that many authors have attributed bands around 1180–1170 cm^{-1} to NO^- species [16,19,20,32,33]. As we will show (see below) these bands are rather due to nitrite species.

Table 3
Calculated adsorption energy of NO when NO^{n-} species are formed on reduced ceria nanoparticles (species a and b for $n = 1$ and 2) and on reduced $CeO_2(1\,1\,1)$ slab (species c for $n = 2$), $E_{ads}(NO)$ in eV, and characteristic experimental and calculated vibrational frequencies of the species.

Species	$E_{ads}(NO)$, eV[a]	ν, cm^{-1}	Ov_{in}/Ov_{fin}[b]	Ce^{3+},[c]	Isotopic shift after substitution of ^{14}N by ^{15}N, cm^{-1}
$[NO^{2-}]$ (exp.)	–	1010–983	–	–	−17 to −20
$[NO^{2-}]$-a	−1.35	993	2/2	4/2	−18
$[NO^{2-}]$-b	−1.15	979	3/3	6/4	−17
$[NO^{2-}]$-c	−1.60	1005	2/2	4/2	−18
$[NO^{-}]$-a	−0.36	1454	1/1	2/1	−26
$[NO^{-}]$-b	−0.45	1435	2/2	4/3	−26

[a] $E_{ads}(NO)$ is calculated with respect to one NO molecule in the gas phase and reduced ceria with the number of O vacancies shown in the column Ov_{in}.
[b] The number of O vacancies in the model before the adsorption of NO and after the formation of the adsorbed species.
[c] The number of Ce^{3+} ions in the model before the adsorption of NO and after the formation of the adsorbed species.

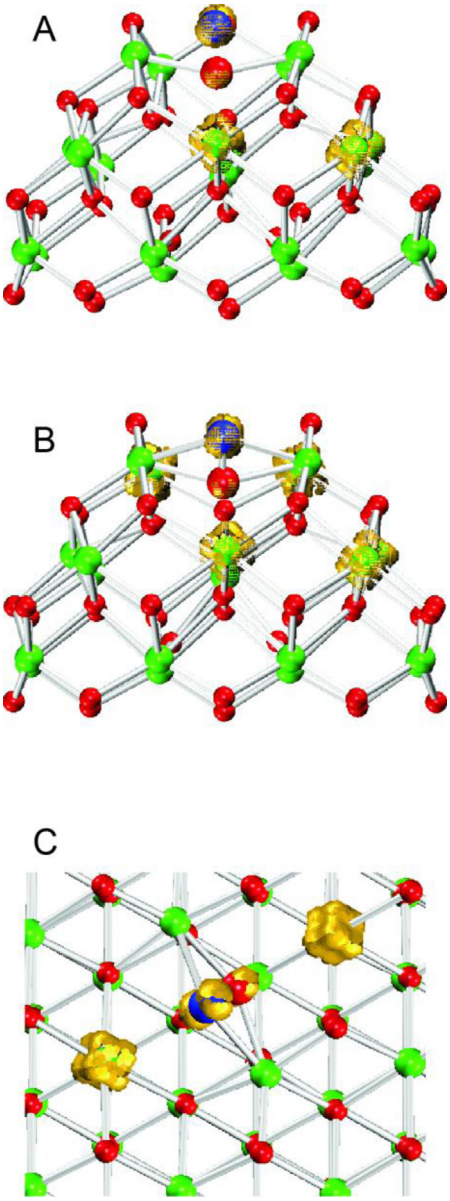

Fig. 5. Optimized structures of NO^{2-}. The structures obtained with DFT modeling are: $[NO^{2-}]$-a (panel A) and $[NO^{2-}]$-b (panel B) on the nanoparticle and $[NO^{2-}]$-c (panel C) on $CeO_2(1\,1\,1)$ surface (colour coding: dark blue – nitrogen, red – oxygen, light green – cerium, yellow – unpaired electron density). (For interpretation of the references to color in this figure legend, the reader is referred to the web version of this article.)

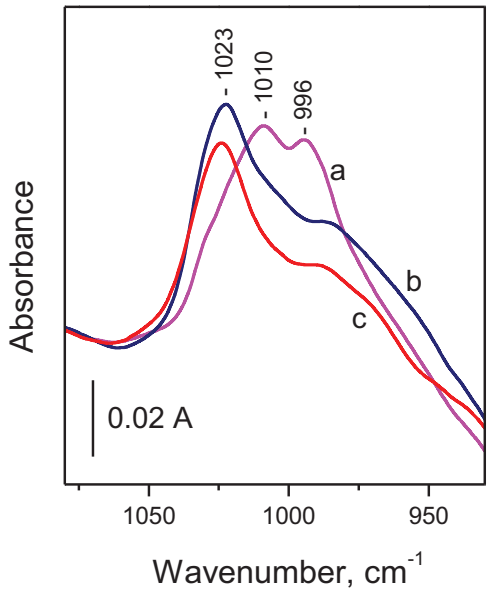

Fig. 6. FTIR spectra of ^{14}NO adsorbed onto the reduced CeO_2(B) sample. Successive adsorption of small NO doses corresponding to 180 (a), and 340 (b) $\mu mol\,g^{-1}$, and under 100 Pa NO equilibrium pressure (c). The spectra are background corrected.

3.6. Reactivity of NO^{2-}

Increase of the amount of NO dosed to reduced CeO_2(B) sample leads to erosion of the bands at 1010 and 996 cm^{-1} and appearance of new bands in the region, with maxima at 1023 and 987 cm^{-1} (Fig. 6). Analysis of the Ce^{3+} band shows that the process starts slightly before the full oxidation of ceria.

The new bands are hardly affected by a further increase in the NO partial pressure although some decrease in their intensity with the increase of the amount of NO added to ceria was observed. The results indicate conversion of NO^{2-} into another species that are observed in the same spectral region. In order to obtain more information on the nature of these new species we analyzed the experiments involving isotopic labeling.

A comparison between the spectra of adsorbed ^{14}NO and ^{15}NO (see Fig. 7, spectra a and b, respectively) shows a very different shape of the IR features which implies that it involves both, N—O and N—N vibrations. Indeed, the results can be rationalized assuming the band at 1023 cm^{-1} consists of two components characterizing N—N and N—O modes, respectively. Upon $^{15}N/^{14}N$ isotopic substitution, the N—O component is shifted to 1002 cm^{-1} while the N—N component, to 988 cm^{-1}. The respective isotopic shift factors (1.021 and 1.035, respectively) are consistent with the supposition. The lower-frequency band (987 cm^{-1}) is shifted

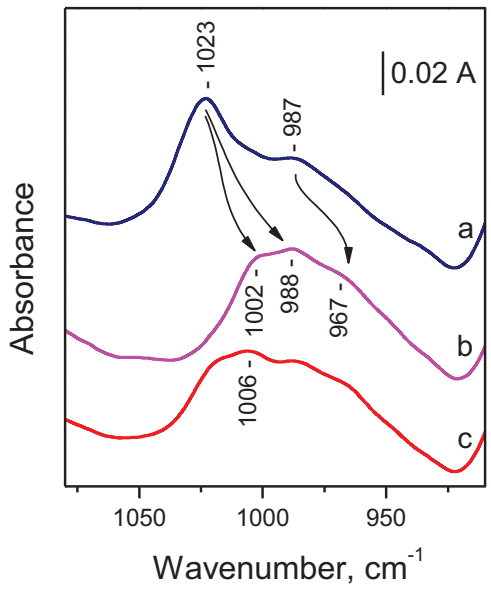

Fig. 7. FTIR spectra of ^{14}NO (a), ^{15}NO (b) and $^{14}NO + ^{15}NO$ (c) adsorbed onto the reduced CeO_2(B) sample. All spectra are background corrected and registered under *ca.* 100 Pa NO equilibrium pressure.

to 967 cm^{-1} and the isotopic shift factor (1.020) indicates the band is due to N—O modes. The proposed model is confirmed by the spectra of co-adsorbed ^{14}NO and ^{15}NO. In this case one should expect appearance of an intense $^{14}N—^{15}N$ band around 1005–1006 cm^{-1} which is indeed observed (Fig. 7, spectrum c).

The existence of IR active N—N bond strongly indicates formation of ONNO-type of species with low symmetry. This low symmetry is responsible for the IR activity of the $^{14}N—^{14}N$ stretching band and the lack of coupling between the two N—O oscillators. We assign the bands at 1023 and 987 cm^{-1} to hyponitrite-like species, $^{14}N_2O_2^{2-}$. Unfortunately, we cannot draw definite conclusions about the presence of higher-frequency concomitant band(s) because at these conditions other species (such as N_2O, surface nitrites and some nitrates) manifesting strong bands in the region are formed (vide infra). Nevertheless, the assignment is consistent with reports concerning matrix-isolated hyponitrites where a band at 1028 cm^{-1} was reported [74]. Similar bands (at 1021 and 974 cm^{-1}) produced after ^{14}NO adsorption on ceria have also been earlier assigned to *cis*-hyponitrites [20,23].

The situation with the CeO_2(A) sample, although similar, shows some differences. When the Ce^{3+} band at 2118 cm^{-1} almost disappeared upon NO dosage, another band at 1008 cm^{-1} started to develop (see Fig. S9 from the Supplementary content). Second derivatives indicate decrease in intensity of the bands at 1003 and 983 cm^{-1} and development of a band at 979 cm^{-1} (in addition to that at 1008 cm^{-1}). Therefore, in this case not only the NO^{2-} bands, but the hyponitrite bands are shifted to lower frequencies as compared to the CeO_2(B) sample. It is also evident that the reactivity of the NO^{2-} species in this case is lower (see the intense residual band at 983 cm^{-1} in the second derivatives presented in Fig. S9 from the Supplementary content). As a result, in this case the detailed analysis of the spectra of labeled molecules is practically impossible.

In order to obtain additional information on the stability and vibrational frequencies of hyponitrites we modeled various structures of $N_2O_2^{2-}$ and $N_2O_2^{-}$ species on ceria nanoparticles in *trans*- and *cis*- configurations (see Fig. 8 and the Supplementary content).

The stability of the modeled hyponitrites varies markedly, from −0.91 to −3.65 eV, and depends mainly on two factors: (i) the location of the species with respect to oxygen vacancy of the nanoparticle, and (i) the charge of the hyponitrites. The most stable $N_2O_2^{2-}$ structures with E_{ads} = −2.49 to −3.65 eV are those in which one of the oxygen or nitrogen atoms of the hyponitrite moiety is located inside or close to the place of an oxygen vacancy (Fig. 8B and C). The charge of the hyponitrite also has substantial influence on its stability: $N_2O_2^{-}$ are less stable than the $N_2O_2^{2-}$ species with the same structure by about one eV. The stability of hyponitrites is not strongly affected by their *trans*- or *cis*-configuration: it is similar for the most stable *trans*- and *cis*-species.

The characteristic vibrational frequencies of the hyponitrites depend on their structure, coordination and charge. More details are given in the Supplementary Content (See Fig. S10 and Table S2 from the Supplementary content) and here we will underline several important conclusions:

- Non-symmetric species are characterized by one N—N and two independent N—O modes. The isotope exchange affects the two N—O modes almost independently, *i.e.*, $O^{14}N^{15}NO$ species will not feature N—O frequencies averaged between those of $O^{14}N^{14}NO$ and $O^{15}N^{15}NO$ species. Due to the anisotropy of the system (presence of the surface), fully symmetric *trans*-hyponitrites species cannot be formed and most *trans*-hyponitrite structures have one NO group side-on coordinated to a cerium ion and the second one coordinated only *via* one of the atoms.
- With increasing symmetry the N—O modes become coupled and this leads to appearance of intermediate N—O modes in the IR spectra of the $O^{14}N^{15}NO$ species. The higher symmetry is more typical for the *cis*-structures.
- The N—N vibrations can be observed in a wide spectral region, 1270–1020 cm^{-1} for *trans*-, and 1321–1247 cm^{-1} for *cis*-$N_2O_2^{2-}$ species. This frequency is the highest one for structures coordinated by the two oxygen atoms. With $N_2O_2^{-}$ species the N—N frequency can fall down to 900 cm^{-1}.
- The N—O frequencies strongly depend on the structure. For non symmetric species having one oxygen not coordinated to the surface the N═O bond is double and the frequency is the highest one.
- The calculated NO frequencies of the $N_2O_2^{-}$ species are higher, and the N—N frequencies lower than the corresponding modes of $N_2O_2^{2-}$ species with the same structure.

Looking back to the experimental results we note the good coincidence between the observed spectra and the structure shown in Fig. 8C. As already noted, in similar structures the N—N stretching frequency could be observed at relatively low wavenumbers.

It is considered that hyponitrites on ceria are produced as a result of the dimerisation of two NO^{-} anions [13,20]. As described above, we have not detected NO^{-}. Our results indicate that hyponitrites are likely produced from NO^{2-} according to the following reaction:

$$-Ce^{4+}-[NO]^{2-}-Ce^{4+}- + NO \rightarrow -Ce^{4+}-[N_2O_2]^{2-}-Ce^{4+}-. \quad (3)$$

Similar interaction has already been reported for NO^{2-} in a di-yttrium complex [73]. DFT calculations based on the structures shown in Fig. 4A and Fig. 8B suggest that the reaction is exothermic with reaction energy of −2.31 eV.

Finally, we report that the hyponitrite species disappear in co-presence of NO and O_2 in the gas phase (details not shown).

3.7. Formation of N_2O

When the 2118 cm^{-1} band (characteristic of Ce^{3+} ions) almost disappeared adsorbed $^{14}N_2O$ was detected (ν_{N-N} at 2234 cm^{-1} and ν_{N-O} at 1257 cm^{-1}). The isotopic labeling experiments prove that N_2O is produced by the coupling of two NO molecules

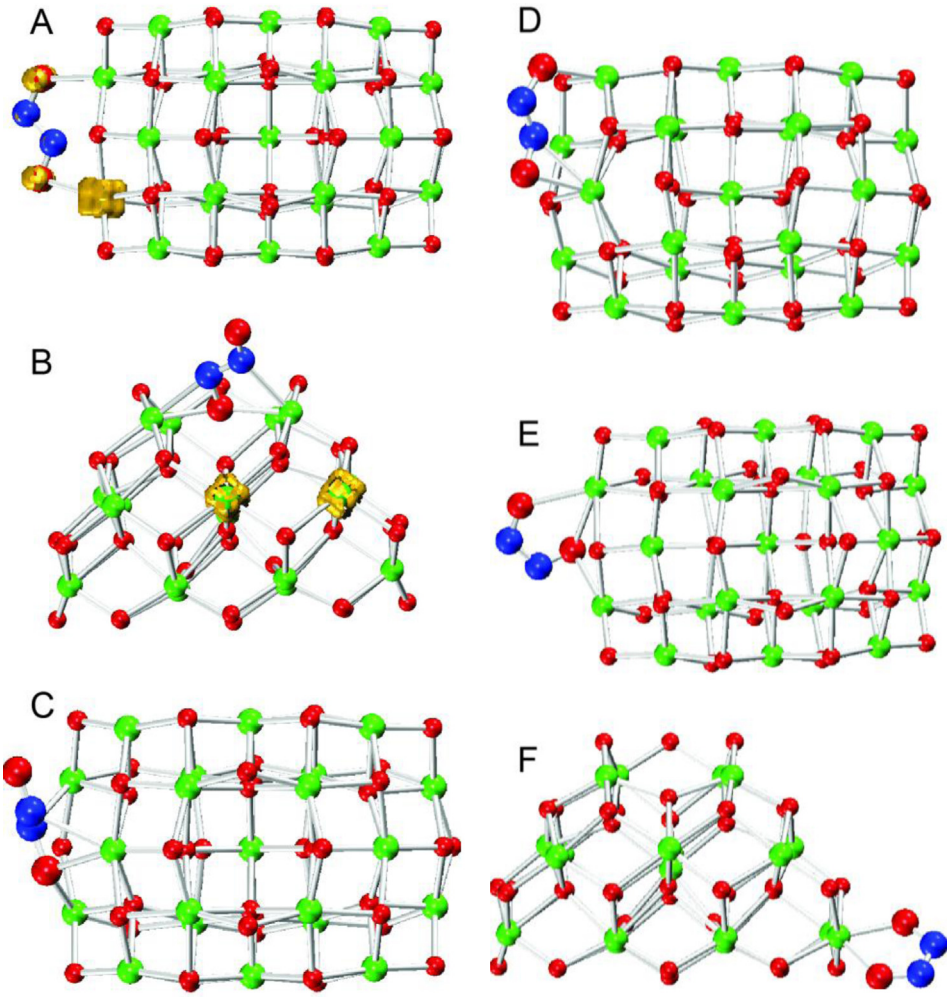

Fig. 8. Examples of optimised structures of hyponitrite species: *trans*-$[N_2O_2]^-$ species (A), *trans*-$[N_2O_2]^{2-}$ species (B, C and D), and *cis*-$[N_2O_2]^{2-}$ species (E and F), on the ceria nanoparticle (colour coding: dark blue – nitrogen, red – oxygen, light green – cerium, yellow – unpaired electron density). (For interpretation of the references to color in this figure legend, the reader is referred to the web version of this article.)

when interacting with ceria and does not originate from N_2O contaminants in NO. Four IR bands with similar intensities are registered after the adsorption of the NO isotopic mixture: 2241 cm^{-1} ($^{14}N_2O$), 2216 cm^{-1} ($^{15}N^{14}NO$), 2196 cm^{-1} ($^{14}N^{15}NO$) and 2170 cm^{-1} ($^{15}N_2O$) (see Fig. S11 from the Supplementary content). Therefore, we suggest that one of the routes for N_2O production is according to the reaction:

$$-Ce^{4+}-[N_2O_2]^{2-}-Ce^{4+}- \rightarrow -Ce^{4+}-O^{2-}-Ce^{4+}- + N_2O. \quad (4)$$

Indeed, as stated above, some decrease in the concentration of the hyponitrite species during NO dosage was established.

Although we detected N_2O only after the principal part of the Ce^{3+} ions disappeared, it seems likely that some N_2O was formed at earlier interaction stages, but has reacted with oxygen vacancies to form N_2:

$$-Ce^{3+}-\square-Ce^{3+}- + N_2O \rightarrow -Ce^{4+}-O^{2-}-Ce^{4+}- + N_2. \quad (5)$$

This supposition is supported by separate experiments that have shown that N_2O easily reoxidizes reduced ceria (for details on the interaction see Fig. S12 from the Supplementary content and the corresponding text).

3.8. Other nitrogen-oxo species

The other species formed under NO equilibrium pressure include surface nitrites characterized by three bands changing in concert, at 1314–1308 (w), 1176–1167 (s) and 825–824 cm^{-1} (w) [71,72] (Fig. S13, panel A). The results of the isotopic studies are consistent with the expected isotopic shifts. Note that nitrites were also detected with non-reduced ceria, *i.e.*, no Ce^{3+} ions are necessary for their formation.

At the final stages of NO adsorption (under NO equilibrium pressure) nitrates characterized by sets of bands in the 1600–1510, 1260–1200 and 1040–1000 cm^{-1} regions were also produced [71].

3.9. Possible role of N_3^- and NO^{2-} in catalysis

In summary, our study involving isotopically labeled species points out that many of the proposed assignments of the nitrogen-oxo species on ceria (see Table 1) should be revised. We have shown that, interacting with reduced ceria, NO can be converted to N_3^- and NO^{2-}, where the formal nitrogen oxidation state is −1/3 and 0, respectively. These species are possible intermediates in the conversion of NO on ceria-based storage–reduction catalysts which operate under periodic switches between lean and rich conditions. They could also be formed during other deNO_x adsorption and catalytic processes, especially when conditions of formation

of reduced ceria are maintained. Indeed, it is believed that reduced sites on ceria in three-way catalysts are directly involved in NO conversion. While azides are inert toward NO and can be converted in co-presence of NO and O_2, the NO^{2-} species easily interact with NO thus producing hyponitrites. The latter decompose to N_2O which, reacting with reduced ceria, produces N_2. Thus, one may speculate that catalysts forming dominantly NO^{2-} species would be more efficient in direct NO decomposition while NO catalytic reduction would be favored with catalysts forming azide species.

The role of metal in storage–reduction catalysts is widely discussed. Among other, it has been found that supported platinum favors the reduction of ceria [53]. Here we have demonstrated that such reduced ceria species react with NO_x even at room temperature leading to the formation of N—N bonds which is a decisive step for the conversion of NO to dinitrogen.

4. Conclusions

We report on two new pathways of NO reductive conversion on ceria. According to one of the pathways, NO reacts with Ce^{3+} ion couples forming NO^{2-} species in η^2:η^2 positions. A second NO molecule reacts with these species thus producing hyponitrites, $[N_2O_2]^{2-}$, and then N_2O. N_2O interacts with reduced ceria forming N_2. The other pathway comprises oxidation of seven Ce^{3+} ions to Ce^{4+} by three NO molecules and formation of surface azides (N_3^-). These azides show remarkable chemical similarity with surface isocyanates: they are highly inert toward NO or O_2 alone but readily interact with a mixture of the two gases. The relative concentrations of N_3^- and NO^{2-} species strongly depend on ceria morphology thus allowing design of adsorbents and catalysts selective to one of the conversion pathways.

Acknowledgments

The authors gratefully acknowledge the financial support by the Bulgarian National Science Fund(project DCVP 02/02) and the FP7 program of the European Union (project Beyond Everest and COST Action CM1104). We also thank the Bulgarian Supercomputer Center for providing computational resources and assistance and the Alexander von Humboldt foundation for scientific donation.

Appendix A. Supplementary data

Supplementary data associated with this article can be found, in the online version, at http://dx.doi.org/10.1016/j.apcatb.2015.03.054.

References

[1] K.C. Taylor, Catal. Rev. Sci. Eng. 35 (1993) 457–481.
[2] V.I. Pârvulescu, P. Grange, B. Delmon, Catal. Today 46 (1998) 233–316.
[3] M. Shelef, Chem. Rev. 95 (1995) 209–225.
[4] W.S. Epling, L.E. Campbell, A. Yezerets, N.W. Currier, J.E. Parks, Catal. Rev. Sci. Eng. 46 (2004) 163–245.
[5] J. Paier, C. Penschke, J. Sauer, Chem. Rev. 113 (2013) 3949–3985.
[6] Y. Arikawa, M. Onishi, Coord. Chem. Rev. 256 (2012) 468–478.
[7] G. Spoto, S. Bordiga, D. Scarano, A. Zecchina, Catal. Lett. 13 (1992) 39–44.
[8] G. Centi, S. Perathoner, Appl. Catal. A: Gen. 132 (1995) 179–250.
[9] Q. Sun, Z.-X. Gao, B. Wen, W.M.H. Sachtler, Catal. Lett. 78 (2002) 1–5.
[10] A. Grossale, I. Nova, E. Tronconi, Catal. Lett. 30 (2009) 525–531.
[11] S. Kameoka, T. Chafik, Y. Ukisu, T. Miyadera, Catal. Lett. 55 (1998) 211–215.
[12] K. Hadjiivanov, H. Knözinger, B. Tsyntsarski, L. Dimitrov, Catal. Lett. 62 (1999) 35–40.
[13] A. Trovarelli, Catal. Rev. Sci. Eng. 38 (1996) 439–520.
[14] Z. Say, E.I. Vovk, V.I. Bukhtiyarov, E. Ozensoy, Appl. Catal. B: Environ. 142–143 (2013) 89–100.
[15] A. Filtschew, D. Stranz, C. Hess, Phys. Chem. Chem. Phys. 15 (2013) 9066–9069.
[16] G. Qi, R.T. Yang, R. Chang, Appl. Catal. B: Environ. 51 (2004) 93–106.
[17] M. Daturi, N. Bion, J. Saussey, J.-C. Lavalley, C. Hedouin, T. Seguelong, G. Blanchard, Phys. Chem. Chem. Phys. 3 (2001) 252–255.
[18] N. Zouaoui, M. Issa, D. Kehrli, M. Jeguirim, Catal. Today 189 (2012) 65–69.
[19] L. Zhang, J. Pirce, V. Leung, D. Wang, W.S. Epling, J. Phys. Chem. C 117 (2013) 8282–8289.
[20] A. Martínez-Arias, J. Soria, J.C. Conesa, X.L. Seoane, A. Arcoya, R.L. Cataluña, J. Chem. Soc. Faraday Trans. 91 (1995) 1679–1687.
[21] M. Niwa, Y. Furukawa, Y. Murakami, J. Colloid Interface Sci. 86 (1982) 260–265.
[22] R. Cataluña, A. Arcoya, X.L. Seoane, A. Martínez-Arias, J.M. Coronado, J.C. Conesa, J. Soria, L.A. Petrov, Stud. Surf. Sci. Catal. 96 (1995) 215–227.
[23] S. Philipp, A. Drochner, J. Kunert, H. Vogel, J. Theis, E.S. Lox, Top. Catal. 30/31 (2004) 235–238.
[24] S. Yang, Y. Guo, H. Chang, L. Ma, Y. Peng, Z. Qu, N. Yan, C. Wang, J. Li, Appl. Catal. B: Environ. 136–137 (2013) 19–28.
[25] A.N. Il'ichev, M.D. Shibanova, A.A. Ukharskii, A.M. Kulizade, V.N. Korchak, Kinet. Catal. 46 (2005) 387–395.
[26] B. Azambre, I. Atribak, A. Bueno-López, A. García-García, J. Phys. Chem. C 114 (2010) 13300–13312.
[27] L. Liu, Y. Cao, W. Sun, Z. Yao, B. Liu, F. Gao, L. Dong, Catal. Today 175 (2011) 48–54.
[28] A. García-García, A. Bueno-López, Catal. Sci. Ser., Catalysis by Ceria and Related Materials, 2nd Ed., (Trovarelli, A.; Fornasiero, P., Eds.), 12, (2013), 223–246.
[29] M.O. Symalla, A. Drochner, H. Vogel, S. Philipp, U. Göbel, W. Müller, Top. Catal. 42–43 (2007) 199–202.
[30] M. Haneda, T. Morita, Y. Nagao, Y. Kintaichi, H. Hamada, Phys. Chem. Chem. Phys. 3 (2001) 4696–4700.
[31] S.H. Overbury, D.R. Mullins, D.R. Huntley, L. Kundakovic, J. Catal. 186 (1999) 296–309.
[32] M. Kantcheva, O. Samarskaya, L. Ilieva, G. Pantaleo, A.M. Venezia, D. Andreeva, Appl. Catal. B: Environ. 88 (2009) 113–126.
[33] L. Xu, X.L. Li, M. Crocker, Z.S. Zhang, A.M. Zhu, C. Shi, J. Mol. Catal. A: Chem. 378 (2013) 82–90.
[34] B. Azambre, L. Zenboury, A. Koch, J.V. Weber, J. Phys. Chem. C 113 (2009) 13287–13299.
[35] Y. Peng, C. Liu, X. Zhang, J. Li, Appl. Catal. B: Environ. 140–141 (2013) 276–282.
[36] L. Liu, J. Cai, L. Qi, Q. Yu, K. Sun, B. Liu, F. Gao, L. Dong, Y. Chen, J. Mol. Catal. A: Chem. 327 (2010) 1–11.
[37] A. Adamski, E. Tabor, B. Gil, Z. Sojka, Catal. Today 119 (2007) 114–119.
[38] A. Adamski, G. Djéga-Mariadassou, Z. Sojka, Catal. Today 119 (2007) 120–124.
[39] L. Wang, R. Ran, X. Wu, M. Li, D.J. Weng, Rare Earths 31 (2013) 1074–1080.
[40] N. Drenchev, I. Spassova, E. Ivanova, M. Khristova, K. Hadjiivanov, Appl. Catal. B: Environ. 138–139 (2013) 362–372.
[41] R. Zhang, Q. Zhong, W. Zhao, L. Yu, H. Qu, Appl. Surf. Sci. 289 (2014) 237–244.
[42] Z.M. El-Bahy, Modern Res. Catal. 2 (2013) 136–147.
[43] L. Chen, Z. Si, Z. Wu, D. Weng, ACS Appl. Mater. Inter. 6 (2014) 8134–8145.
[44] M. Konsolakis, Chem. Eng. J. 183 (2012) 550–551.
[45] M. Radlik, M. Adamowska, A. Łamacz, A. Krzton, P. Da Costa, W. Turek, React. Kinet. Mech. Catal. 109 (2013) 43–56.
[46] A.M. Hernández-Giménez, D. Lozano-Castelló, A. Bueno-López, Appl. Catal. B: Environ. 148–149 (2014) 406–414.
[47] C. Kladis, S.K. Bhargava, K. Foger, D.B. Akolekar, J. Mol. Catal. A: Chem. 175 (2001) 241–248.
[48] F. Cao, J. Xiang, S. Su, P. Wang, L. Sun, S. Hu, S. Lei, Chem. Eng. J. 243 (2014) 347–354.
[49] S. Liu, X. Wu, Y. Lin, M. Li, D. Weng, Chin. J. Catal. 35 (2014) 407–415.
[50] J. Szanyi, J.H. Kwak, Chem. Commun. 50 (2014) 14998–15001.
[51] C. Binet, A. Badri, J.-C. Lavalley, J. Phys. Chem. 98 (1994) 6392–6398.
[52] K. Hadjiivanov, M. Mihaylov, D. Panayotov, E. Ivanova, K. Chakarova, Spectrosc. Prop. Inorg. Organomet. Compd. 45 (2014) 43–78.
[53] G.N. Vayssilov, Y. Lykhach, A. Migani, T. Staudt, G.P. Petrova, N. Tsud, T. Skála, A. Bruix, F. Illas, K.C. Prince, V. Matolín, K.M. Neyman, J. Libuda, Nat. Mater. 10 (2011) 310–315.
[54] A. Migani, G.N. Vayssilov, S.T. Bromley, F. Illas, K.M. Neyman, J. Mater. Chem. 20 (2010) 10535–10546.
[55] G.N. Vayssilov, M. Mihaylov, P.S. Petkov, K.I. Hadjiivanov, K.M. Neyman, J. Phys. Chem. C 115 (2011) 23435–23454.
[56] K. Hadjiivanov, Adv. Catal. 57 (2014) 99–318.
[57] A. Badri, C. Binet, J.C. Lavalley, J. Chem. Soc. Faraday Trans. 92 (1996) 4669–4673.
[58] M. Daturi, E. Finocchio, C. Binet, J.C. Lavalley, F. Fally, V.J. Perrichon, Phys. Chem. B 103 (1999) 4884–4891.
[59] S. Agarwal, L. Lefferts, B.L. Mojet, ChemCatChem 5 (2013) 479–489.
[60] R. Farra, S. Wrabetz, M.E. Schuster, E. Stotz, N.G. Hamilton, A.P. Amrute, J. Pérez-Ramírez, N. López, D. Teschner, Phys. Chem. Chem. Phys. 15 (2013) 3454–3465.
[61] M.G. Samant, R. Viswanathan, H. Seki, P.S. Bagus, C.J. Nelin, M.R. Philpott, J. Chem. Phys. 89 (1988) 583–589.
[62] Q. Zhong, D.A. Steinhurst, E.E. Carpenter, J.C. Owrutsky, Langmuir 18 (2002) 7401–7408.
[63] Z. Dori, R.F. Ziolo, Chem. Rev. 73 (1973) 247–254.
[64] H.A. Papazian, J. Chem. Phys. 34 (1961) 1614–1616.
[65] M.Y. Mihaylov, E.Z. Ivanova, H.A. Aleksandrov, P. St Petkov, G.N. Vayssilov, K.I. Hadjiivanov, Chem. Commun. 51 (2015) 5668–5671.

[66] B. Bonelli, B. Civalleri, B. Fubini, P. Ugliengo, C. Otero Areán, E. Garrone, J. Phys. Chem. B 104 (2000) 10978–10988.
[67] T. Montanari, G. Busca, Vibr. Spectrosc. 46 (2008) 45–51.
[68] J. Kritzenberger, E. Jobson, A. Wokaun, A. Baiker, Catal. Lett. 5 (1990) 73–80.
[69] G. Ramis, L. Yi, G. Busca, Catal. Today 28 (1996) 373–380.
[70] N. Bion, J. Saussey, M. Haneda, M. Daturi, J. Catal. 217 (2003) 47–58.
[71] K. Hadjiivanov, Catal. Rev. Sci. Eng. 42 (2000) 71–144.
[72] J. Laane, J.R. Ohlsen, Progr. Inorg. Chem. 27 (1980) 465–513.
[73] W.J. Evans, M. Fang, J.E. Bates, F. Furche, J.W. Ziller, M.D. Kiesz, J.I. Zink, Nature Chem. 2 (2010) 644–647.
[74] L. Andrews, B. Jiang, J. Am. Chem. Soc. 109 (2001) 177–185.